Antenna Cross-Polarization Isolation and Calibration of Hybrid-Polarization Radars

Thomas J. Miller, *Member, IEEE*, Ozlem Kilic, *Senior Member, IEEE*, and Mark S. Mirotznik, *Senior Member, IEEE*

***Abstract*—This letter presents an experiment using a fully polarimetric hybrid-polarization (CL-pol) radar that employs separate spiral antennas for transmit of the orthogonal circular polarizations and operates from 8 to 16 GHz. We propose a model for the antenna cross-polarization isolation (XPI) and calibration of this radar. The transmit XPI is characterized by leveraging the Doppler shift caused by a continually rotating dihedral target illuminated by a circularly polarized wave. Experimental results show the validity of the radar model and antenna measurement technique.**

***Index Terms*—Antenna measurements, crosstalk, radar cross section, radar polarimetry.**

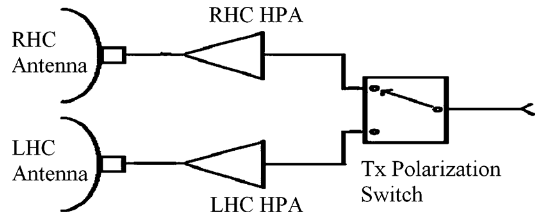

Fig. 1. Radar front-end transmit circuit. The signal passes through a transmit switch that selects either the left-hand circular polarization path or the right-hand circular polarization path. After the switch, the signal passes through a digitally controlled RF amplifier and then goes on to the transmit antenna, which generates the desired polarization.

I. Introduction

ANTENNA cross-polarization isolation (XPI) can have adverse effects on polarimetric remote sensing. Touzi *et al.* [1] investigated the impact of XPI on polarimetric maritime surveillance applications. One method applied to the mitigation of XPI is the use of hybrid-polarity architecture (CL-pol) [2], where the radar transmits circular polarizations and receives linear polarizations. Raney *et al.* document the advantages of CL-pol in [2]–[4].

In October 2011, an instrumentation radar was set up to measure fully polarimetric CL-pol data and placed in the Maneuvering and Seakeeping Basin (MASK) at the Naval Surface Warfare Center, Carderock Division (NSWCCD) in West Bethesda, MD, USA [5]. Radar cross section (RCS) measurements were made of a variety of targets, including a dihedral, a sphere, water wave clutter, water wave induced multipath, and a life raft. The objective was to obtain a fully polarimetric calibrated data set of controlled scenes representative of ocean remote-sensing scenes. These data are meant to help investigate and validate models of the polarimetric effects in the measured scenes.

The instrumentation radar used in the NSWCCD experiment consisted of a Star Dynamics Blue Max Gen4 radar core, with a custom front-end architecture attached. Blue Max radars are coherent stepped-frequency instrumentation radars using superheterodyne receivers and can be programmed to execute a variety of waveforms. The waveform relevant for this document started at 8.0 GHz and stepped through an 8.984375-GHz chirp bandwidth in 512 steps with a Δf of 1.5625 MHz. Polarizations were handled sequentially, and the overall burst repetition frequency (BRF) was $\sim$105 chirps/s. We believe this is the first example of a fully polarimetric X/Ku-band CL-pol radar published in literature.

System [3] and polarization decomposition models [6] for prior examples of CL-pol radars, the mini-radio frequency (mini-RF) radars of the Chandrayaan-1, and the Lunar Reconnaissance Orbiter (LRO) [3] were for compact polarimetry. The fully polarimetric system models of Freeman *et al.* in [7]–[9] are for polarimeters that both transmit and receive linear polarizations (LL-pol). In this letter, we adapt Freeman's proven polarimeter models to our CL-pol radar, and then leverage the model in a novel experiment to evaluate the XPI generated by our spiral transmit antennas.

II. System Model

Fig. 1 depicts the front-end transmit path of the NSWCCD radar. The transmit polarization switch that selects either the right-hand circular polarization (RHC) path or the left-hand circular polarization (LHC) path was tested and shown to have isolation better than 50 dB. The transmit amplifiers in the two paths were identical solid-state high-powered amplifiers (HPAs) that used high-speed control signals to gate the amplifiers for transmission of the RF pulse. In the absence of a positive control gating signal, the amplifier would not transmit. Testing showed this leads to an effective circuit polarization isolation of at least 80 dB at the output of the transmit amplifiers. Having separate amplifiers for the two transmission paths introduced some independence of gain drift between the polarization channels, which needs to be properly handled in post-processing. The transmit antennas were nonidentical in design, with the RHC transmit antenna a spiral antenna, and the LHC antenna a cavity-backed spiral with nonidentical gains. The axial-ratio specification for

Manuscript received June 28, 2013; revised August 22, 2013; accepted September 03, 2013. Date of publication September 17, 2013; date of current version October 01, 2013. This work was supported in part by the Office of Naval Research.

T. Miller is with the Naval Surface Warfare Center, Carderock Division, West Bethesda, MD 20817 USA (e-mail: thomas.j.miller1@navy.mil).

O. Kilic is with the Catholic University of America, Washington, DC 20064 USA (e-mail: kilic@cua.edu).

M. Mirotznik is with the University of Delaware, Newark, DE 19716 USA (e-mail: mirotzni@ece.udel.edu).

Digital Object Identifier 10.1109/LAWP.2013.2282251

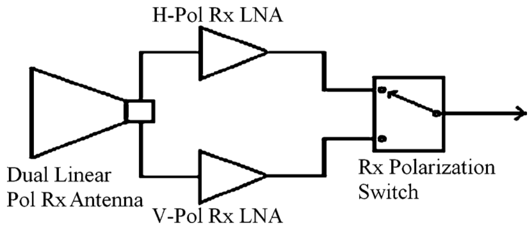

Fig. 2. Radar front-end receive circuit. The signal arrives at the dual linearly polarized receive antenna , and then each polarization passes to separate low noise amplifiers. After the low noise amplifiers, the receive polarization switch selects which polarization is passed to the single-channel radar receiver.

the transmit antennas was ≤ 2.0 dB. According to [10], an elliptically polarized wave can be resolved as two circularly polarized waves of opposite sense, with differing magnitudes and phases. From [11], the axial ratio is calculated by

$$r = \frac{\rho_{\mathrm{C}} + 1}{\rho_{\mathrm{C}} - 1} \tag{1}$$

$$\hat{\rho}_{\mathrm{C}} = \frac{\hat{E}_{\mathrm{R}}}{\hat{E}_{\mathrm{L}}} = \rho_{\mathrm{C}} e^{j\delta_{\mathrm{C}}} \tag{2}$$

where, per the notation of [11], the ^ above a variable denotes a complex number, r is the axial ratio, $\hat{E}_{\mathrm{R}}$ is the complex RHC field produced by the antenna, $\hat{E}_{\mathrm{L}}$ is the complex LHC field produced by the antenna, ρ_{C} is the magnitude of the ratio of the orthogonal circular fields, and δ_{C} is the relative phase. Based on (1) and (2), an axial-ratio specification of ≤ 2.0 dB corresponds to an XPI signal ≤ 18.8 dB below the desired signal. Therefore, the transmit XPI experienced by the radar is dominated by the ellipticity of the transmit antennas.

Fig. 2 depicts the front-end receive polarization path. The dual linearly polarized horn receive antenna had slightly differing gains in the horizontal and vertical polarizations. Port-to-port isolation of the receive antenna was measured to be better than 32 dB in the frequency band of interest. The receive amplifiers were identical solid-state low noise amplifiers (LNAs). Again, having separate amplifiers for the two transmission paths introduced some independence of drift between the two channels that will need to be handled in post-processing. The receive polarization switch was identical to the transmit polarization switch and was also shown to have better than 50 dB isolation. We conclude that the receive XPI experienced by this radar is dominated by the port-to-port isolation of the dual-polarization receive antenna.

Based on the radar front-end circuit characteristics, we chose to modify Freeman's model from [9], removing the Faraday rotation term, shifting the transmit matrices based on the implemented circuit, and adding drift compensation terms similar to [7]

$$\begin{aligned} M = {} & \alpha_0 A e^{j\phi} \begin{pmatrix} 1 & \delta_2 \\ \delta_1 & 1 \end{pmatrix} \begin{pmatrix} 1 & 0 \\ 0 & \alpha_1 f_1 \end{pmatrix} \begin{pmatrix} S_{rh} & S_{lh} \\ S_{rv} & S_{lv} \end{pmatrix} \\ & \times \begin{pmatrix} 1 & \delta_3 \\ \delta_4 & 1 \end{pmatrix} \begin{pmatrix} 1 & 0 \\ 0 & \alpha_2 f_2 \end{pmatrix} + N \end{aligned} \tag{3}$$

or

$$M = R'ST.$$

In (3), S represents the target polarimetric scattering matrix, R the system receive matrix, T the system transmit matrix, N the noise signal received in each channel, f_2 is the typical gain imbalance between the RHC and LHC polarization channels, α_2 is the change in f_2 due to independent transmit amplifier drift, δ_3 is the transmit XPI representing RHC transmission from the LHC antenna, δ_4 is the transmit XPI representing LHC transmission from the RHC antenna, f_1 is the typical gain imbalance between the horizontal and vertical polarization receive paths, α_1 is the change in f_1 due to independent receive amplifier drift, δ_2 is the receive XPI factor representing the receipt of vertical polarization when receipt of horizontal was desired, δ_1 is the receive XPI factor for the receipt of horizontal polarization when receipt of vertical polarization was desired, $Ae^{j\phi}$ is the distortion in the RHC transmit, horizontal receive (RH) polarization channel, and α_0 is the change in A due to amplifier gain drift. The transmit XPI factors are related to the complex circular polarization ratio of the individual antenna by

$$\delta_3 = \frac{\hat{E}_{\mathrm{R}}}{\hat{E}_{\mathrm{L}}} = \hat{\rho}_{\mathrm{C}} \tag{4}$$

$$\delta_4 = \frac{\hat{E}_{\mathrm{L}}}{\hat{E}_{\mathrm{R}}} = \frac{1}{\hat{\rho}_{\mathrm{C}}}. \tag{5}$$

III. System Parameter Characterization

Polarization scattering matrices (PSMs) for known targets are required to calibrate and characterize system parameters. PSM's of targets for LL-pol are well known [12]. The following equations [2] are used for transforming LL-pol PSMs to CL-pol PSMs:

$$S_{\mathrm{rh}} = \frac{1}{\sqrt{2}}(S_{\mathrm{hh}} - jS_{\mathrm{vh}}) \tag{6i}$$

$$S_{\mathrm{rv}} = \frac{1}{\sqrt{2}}(S_{\mathrm{hv}} - jS_{\mathrm{vv}}) \tag{6ii}$$

$$S_{\mathrm{lh}} = \frac{1}{\sqrt{2}}(S_{\mathrm{hh}} + jS_{\mathrm{vh}}) \tag{6iii}$$

$$S_{\mathrm{lv}} = \frac{1}{\sqrt{2}}(S_{\mathrm{hv}} + jS_{\mathrm{vv}}). \tag{6iv}$$

Combining the LL-pol PSM for a dihedral from [12] with (6), one obtains

$$\begin{bmatrix} S_{\mathrm{rh}} & S_{\mathrm{lh}} \\ S_{\mathrm{rv}} & S_{\mathrm{lv}} \end{bmatrix} = \frac{1}{\sqrt{2}} \begin{bmatrix} e^{-j2\varphi} & e^{j2\varphi} \\ je^{-j2\varphi} & -je^{j2\varphi} \end{bmatrix}. \tag{7}$$

In (7), the angle φ is defined in [12] as the angle between the dihedral's spine and horizontal polarization.

Combining (7) with (3), the measurement of a dihedral in RH polarization is shown to be

$$\begin{aligned} M_{\mathrm{rh}}^{d} = {} & \underbrace{\frac{\alpha_0 A e^{j\phi}}{\sqrt{2}} e^{-j2\varphi}(1 + j\delta_2\alpha_1 f_1)\sqrt{\sigma}}_{\mathrm{part1}} \\ & + \underbrace{\frac{\alpha_0 A e^{j\phi}}{\sqrt{2}} e^{j2\varphi}(\delta_4 - j\delta_2\alpha_1 f_1\delta_4)\sqrt{\sigma}}_{\mathrm{part2}} + N_{\mathrm{rh}}. \end{aligned} \tag{8}$$

Part 1 of (8) contains the desired S_{rh} signal with receive XPI, and Part 2 of (8) contains only factors related to the transmit XPI. If a dihedral pointed toward the radar being calibrated was set to continually rotate in the h/v plane, then the effective Doppler shift of the $e^{-j2\varphi}$ and $e^{j2\varphi}$ would separate the two parts of (8). The desired signal contained in Part 1 of (8) would additionally be Doppler shifted away from any structure or background clutter at zero Doppler, and the noise term N would also be distributed and reduced. This makes a continually rotating dihedral an attractive target for calibration and for evaluating XPI in the CL-polarization basis. Ignoring the noise terms, the signals that are obtained by measuring a continually rotating dihedral are summarized as

$$M^d_{\rm rh} = \tilde{A}[e^{-j2\varphi}(1+j\delta_2\alpha_1 f_1) + e^{j2\varphi}(\delta_4 - j\delta_2\alpha_1 f_1\delta_4)] \tag{9i}$$

$$M^d_{\rm rv} = \tilde{A}[e^{-j2\varphi}(\delta_1+j\alpha_1 f_1) + e^{j2\varphi}(\delta_1\delta_4 - j\alpha_1 f_1\delta_4)] \tag{9ii}$$

$$\begin{aligned} M^d_{\rm lh} = \tilde{A}[&e^{-j2\varphi}(\delta_3\alpha_2 f_2 + j\delta_2\alpha_1 f_1\delta_3\alpha_2 f_2) \\ &+ e^{j2\varphi}(\alpha_2 f_2 - j\delta_2\alpha_1 f_1\alpha_2 f_2)] \end{aligned} \tag{9iii}$$

$$\begin{aligned} M^d_{\rm lv} = \tilde{A}[&e^{-j2\varphi}(\delta_1\delta_3\alpha_2 f_2 + j\alpha_1 f_1\delta_3\alpha_2 f_2) \\ &+ e^{j2\varphi}(\delta_1\alpha_2 f_2 - j\alpha_1 f_1\alpha_2 f_2)] \end{aligned} \tag{9iv}$$

where $\tilde{A} = \alpha_0 A e^{j\phi}\sqrt{\sigma/2}$

In (9), σ is the RCS of the dihedral. Using Doppler filtering, assuming the amplifier drift terms $\alpha_1 \sim \alpha_2 \sim 1$, assuming the antenna gain balance terms $f_1 \sim f_2 \sim 1$, and assuming the receive XPI terms $\delta_1 \sim \delta_2 \ll 1$, the transmit XPI can be obtained by taking the ratios of different quantities from (9). Testing of the amplifiers validated the $\alpha_1 \sim \alpha_2 \sim 1$ assumption. We believe the $f_1 \sim f_2 \sim 1$ assumption is reasonable based on inspection of the antenna manufacturer test reports. Given the receive antenna's port-to-port isolation of better than 32 dB, we believe $\delta_1 \sim \delta_2 \ll 1$ is also a reasonable assumption. Thus

$$\delta_4 \approx \frac{M^{d+}_{\rm rh}}{M^{d-}_{\rm rh}} \tag{10i}$$

$$\delta_4 \approx -\frac{M^{d+}_{\rm rv}}{M^{d-}_{\rm rv}} \tag{10ii}$$

$$\delta_3 \approx \frac{M^{d-}_{\rm lh}}{M^{d+}_{\rm lh}} \tag{10iii}$$

$$\delta_3 \approx -\frac{M^{d-}_{\rm lv}}{M^{d+}_{\rm lv}}. \tag{10iv}$$

The $d\pm$ superscripts in (10) indicate either a positive or negative Doppler shifted signal. The equivalency of (10i) to (10ii) and of (10iii) to (10iv) can be used to check the underlying assumptions used to obtain (10) from (9). It is important to note that when evaluating the phase in (10), the phase angle derived is dependent upon the rotation angle of the dihedral

$$\delta_4 \propto \frac{e^{j2\varphi}}{e^{-j2\varphi}} \tag{11i}$$

$$\delta_3 \propto \frac{e^{-j2\varphi}}{e^{j2\varphi}}. \tag{11ii}$$

Therefore the phase evaluation of δ_4 and δ_3 is valid when $e^{-j2\varphi} = e^{j2\varphi}$, which occurs when $\varphi = 0, 90, 180$, or 270.

Characterization of the δ_3 and δ_4 factors is obtained by measuring a continually rotating dihedral. The data is then Doppler processed by taking the inverse fast Fourier transform (IFFT) in time over slightly less than the entire file. The exact number of samples included in the IFFT is selected for the sharpest response at the Doppler shift induced by the dihedral. Then, the Doppler spectrum of interest is filtered and FFT'd to return it to the frequency domain. This filtered data is then evaluated using (10) with the α factors set to 1.

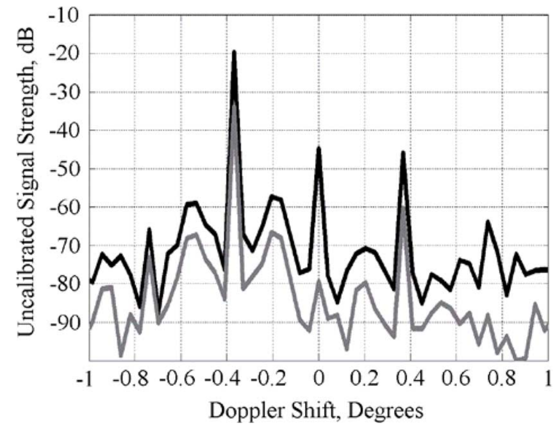

Fig. 3. Doppler spectrum data of a rotating dihedral, RH polarization. The black line indicates the 8-GHz signal, and the gray line the 16-GHz signal.

The same process and assumptions are used to obtain the factors for calibration. From (9), it can be shown that

$$\alpha_0 A e^{j\phi} \approx M^{d-}_{\rm rh}\sqrt{\frac{2}{\sigma}} \tag{12i}$$

$$\alpha_1 f_1 \approx -j\frac{M^{d-}_{\rm rv}}{M^{d-}_{\rm rh}} \tag{12ii}$$

$$\alpha_2 f_2 \approx \frac{M^{d+}_{\rm lh}}{M^{d-}_{\rm rh}} \tag{12iii}$$

$$\alpha_1 f_1 \alpha_2 f_2 \approx j\frac{M^{d+}_{\rm lv}}{M^{d-}_{\rm rh}}. \tag{12iv}$$

Initial calibration is conducted using the same process described to characterize the δ_3 and δ_4 factors, with the α factors set to 1. Secondary calibrations are then used to track the changes in the α factors over time.

IV. Results of System Parameter Measurement

A rotating 8-in-wide × 12-in-tall dihedral was placed in front of the radar in the MASK. The dihedral's rotation was counterclockwise when viewed from the radar, at a rate of $\sim$19.5°/s. Combined with the radar BRF of $\sim$105 chirps/s, and considering the factor of 2 in the $e^{\pm j2\varphi}$ factors of the dihedral CL PSM, we predicted a frequency independent phase shift of $-0.37°$ for an RHC illuminating wave and $+0.37°$ for an LHC. From this point, our discussion will focus on the RHC antenna results, but the conclusions are equally true for the LHC antenna results.

In Fig. 3, the primary RHC signal can be seen at $-0.37°$ of Doppler shift. The LHC XPI from the RHC antenna can be seen at $+0.37°$ of Doppler shift. Building and structure interference is observed at 0 Doppler. The frequency independence of the observed Doppler shift confirms the effects are due to the rotating dihedral's response to the desired RHC and undesired LHC XPI signal. Measuring the antenna in this manner therefore accurately determines the sense of polarization of the antenna under test.

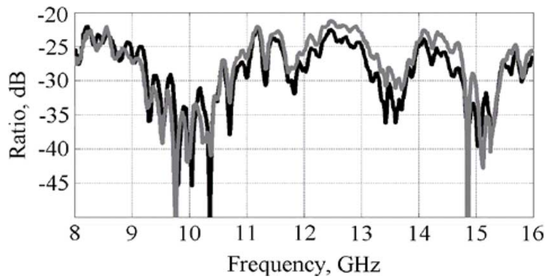

Fig. 4. Measurement of $|\delta_4|$. The black line indicates the measurement according to (10i), and the gray line the measurement according to (10ii).

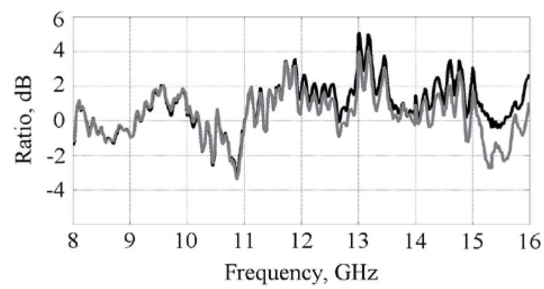

Fig. 5. Measurement of $|f_1 f_2|$. The black line indicates the assessment of (12iv), and the gray line indicates the assessment according to (12ii) × (12iii).

TABLE I
ACCURACY OF RH CALIBRATED RCS AND DRIFT OF THE α-FACTORS OVER TIME

Parameter /Sample	Day 1 06:45	Day 1 10:08	Day 1 15:15	Day 1 16:46	Day 1 18:00
RH Δσ (dB)	+0.3	-0.1	+0.0	-0.1	-0.3
α_0 (dB)	0.0	0.0	0.0	0.0	0.0
α_1 (dB)	-0.0	-0.1	+0.1	+0.0	+0.1
α_2 (dB)	-0.4	-0.1	+0.0	-0.1	-0.1
Parameter /Sample	Day 2 06:44	Day 2 09:20	Day 2 12:56	Day 2 14:09	Day 2 15:56
RH Δσ (dB)	+0.2	-0.1	+0.0	-0.3	+0.0
α_0 (dB)	-1.0	-1.0	-1.0	-1.0	-1.0
α_1 (dB)	+0.1	+0.1	-0.0	-0.1	-0.0
α_2 (dB)	-0.5	-0.5	-0.3	-0.2	-0.1

When analyzing Doppler shifted signals, I and Q imbalances in coherent radar receivers can cause the appearance of a smaller Doppler signal at the opposite sense Doppler from the main signal, or ghosting. We implemented corrections for the system I and Q imbalances of our radar per [13] and verified that all Doppler ghost signals were at least 50 dB suppressed.

In Fig. 4, we compare the (10i) and (10ii) magnitude measurements of δ_4. The slight differences between these measurements can be explained by the radar receiver's linearity specification [14], coherent interference [15] from the -50-dB Doppler ghosting signal, and the receive XPI terms we ignored going from (9) to (10).

In Fig. 5, we compare the (12ii) $\times$ (12iii) and (12iv) magnitude measurements of $f_1 \times f_2$. The explanation for the slight differences between these measurements is the same as that outlined for Fig. 4.

In Table I, we display the results of using a 10-in-radius sphere to assess the accuracy of the wideband RCS in RH polarization and α-factor drift over time. We observe that system drift is dominated by the α_0 and α_2 factors, which characterize the drift due to the HPA transmit amplifiers.

From Table I, we are also able to conclude that, thanks to the use of the α-factors to account for system drift, the calibration accuracy is ± 0.3 dB.

V. CONCLUSION

We presented a model for the calibration and study of XPI in fully polarimetric CL-pol radars. We leveraged this model and the induced Doppler shifts of a continually rotating dihedral illuminated by an elliptically polarized wave to assess the transmit XPI of our radar. The experimental results confirm the validity of the radar calibration and XPI model and the antenna measurement technique.

ACKNOWLEDGMENT

RCS measurement campaigns as described in this letter are large team efforts. The authors would like in particular to thank S. Simmons, B. Good, N. Ildefonso, A. Twichell, H. Barden, J. Neely, B. Crock, D. Morgan, B. Stephens, P. Haldeman, K. Nicolas, B. Fullerton, A. Kurkoski, J. Warfield, and M. Golub-Miller.

REFERENCES

[1] R. Touzi, P. W. Vachon, and J. Wolfe, "Requirement on antenna cross-polarization isolation for the operational use of C-band SAR constellations in maritime surveillance," *IEEE Geosci. Remote Sens. Lett.*, vol. 7, no. 4, pp. 861–865, Oct. 2010.

[2] R. K. Raney, "Hybrid-polarity SAR architecture," *IEEE Trans. Geosci. Remote Sens.*, vol. 45, no. 11, pp. 3397–3404, Nov. 2007.

[3] R. K. Raney, P. D. Spudis, B. Bussey, J. Crusan, J. R. Jensen, W. Marinelli, P. McKerracher, C. Neish, M. Palsetia, R. Schulze, H. B. Sequeira, and H. Winters, "The lunar mini-RF radars: Hybrid polarimetric architecture and initial results," *Proc. IEEE*, vol. 99, no. 5, pp. 808–823, May 2011.

[4] R. K. Raney, A. Freeman, and R. L. Jordan, "Improved range ambiguity performance in quad-pol SAR," *IEEE Trans. Geosci. Remote Sens.*, vol. 50, no. 2, pp. 349–352, Feb. 2012.

[5] T. Miller, O. Kilic, and M. Mirotznik, "Antenna cross-polarization isolation impact on the measurement of weakly cross-polarized sea clutter," in *Proc. IEEE AP/URSI Int. Symp.*, Jul. 2012.

[6] R. K. Raney, J. T. S. Cahill, G. W. Patterson, and D. B. J. Bussey, "The M-Chi decomposition of hybrid dual-polarimetric radar data," in *Proc. IGARSS*, Jul. 2012, pp. 5093–5096.

[7] A. Freeman, "A new system model for radar polarimeters," *IEEE Trans. Geosci. Remote Sens.*, vol. 29, no. 5, pp. 761–767, Sep. 1991.

[8] A. Freeman, J. J. van Zyl, J. D. Klein, H. A. Zebker, and Y. Shen, "Calibration of stokes and scattering matrix format polarimetric SAR data," *IEEE Trans. Geosci. Remote Sens.*, vol. 30, no. 3, pp. 531–539, May 1992.

[9] A. Freeman, "Calibration of linearly polarized polarimetric SAR data subject to faraday rotation," *IEEE Trans. Geosci. Remote Sens.*, vol. 42, no. 8, pp. 1617–1624, Aug. 2004.

[10] J. D. Jackson, *Classical Electrodynamics*, 3rd ed. New York, NY, USA: Wiley, 1998, ch. 7.2.

[11] W. H. Kummer and E. S. Gillespie, "Antenna measurements—1978," *Proc. IEEE*, vol. 66, no. 4, pp. 483–507, Apr. 1978.

[12] J. S. Lee and E. Pottier, *Polarimetric Radar Imaging, From Basics to Applications*. New York, NY, USA: CRC Press, 2009, ch. 3.6.4.

[13] F. E. Churchill, G. W. Ogar, and B. J. Thompson, "The correction of I and Q errors in a coherent processor," *IEEE Trans. Aeros. Electron. Syst.*, vol. AES-17, no. 1, pp. 131–137, Jan. 1981.

[14] STAR Dynamics, Hillard, OH, USA, "BlueMax G6 instrumentation radar system," Accessed Apr. 4, 2013 [Online]. Available: http://www.stardynamics.com/LinkClick.aspx?fileticket=h9rzNkKLWBI%3d&tabid=61

[15] M. I. Skolnik, *Radar Handbook*. New York, NY, USA: McGraw-Hill, 1970, ch. 27.5.